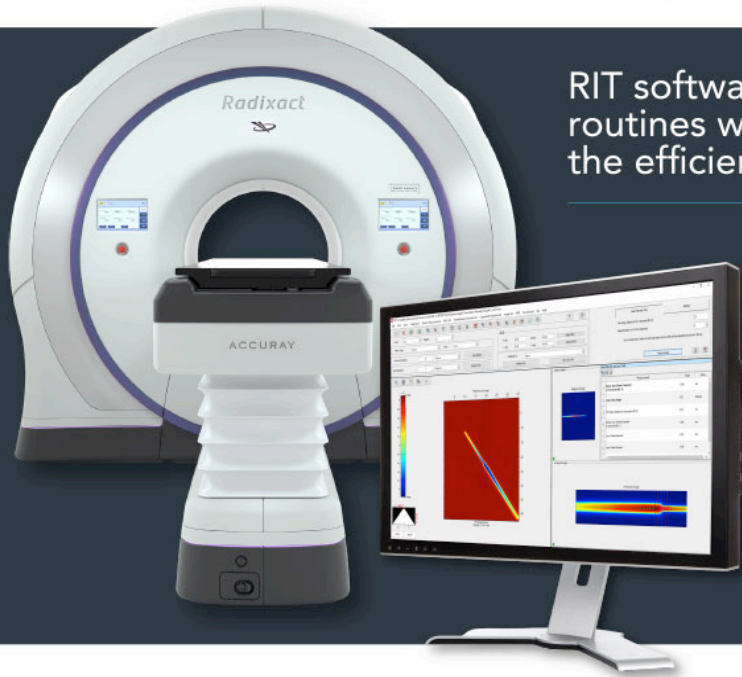


# COMPREHENSIVE TG-148 QA SOLUTIONS

FROM RADIOLOGICAL IMAGING TECHNOLOGY, INC.

RIT offers two software packages for comprehensive TG-148 QA of helical tomotherapy machines. RITG148+ is a precise and state-of-the-art software built to perform all machine and imaging QA measurements for TomoTherapy® and Radixact® treatment delivery systems. RIT Complete adds patient QA capabilities by providing an advanced TomoTherapy Registration feature.

**RITG148+**  
AND  
**RIT Complete**



RIT software's combination of innovative, robust routines with a user-friendly interface to maximize the efficiency and precision of your measurements.

Designed in accordance with TG-148 guidelines, the RITG148+ and RIT Complete software packages analyze the standardized tests and all others recommended for daily, monthly, and annual QA of tomotherapy machines. This includes Static & Rotational Output Consistency, Jaw Centering & Alignment, Overhead Laser Positioning, Interrupted Treatment, and all others recommended for daily, monthly, and annual QA. RITG148+ also analyzes image quality using the tomotherapy cheese phantom.

## Automated QA Tests

- Y-jaw/gantry rotation plane alignment
- Y-jaw divergence/beam centering
- Couch translation/gantry rotation
- Gantry angle consistency
- Treatment field centering
- Interrupted treatment
- MLC alignment test
- Laser localization

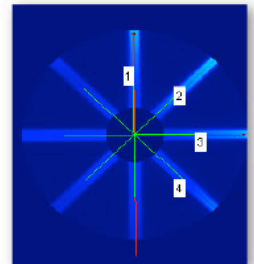
## TomoTherapy® Registration\*

Upgrade to RIT Complete to perform TomoTherapy® patient QA in addition to all the machine and imaging QA tests already included in RITG148+. Easily perform exact dose comparisons using a TomoTherapy® plan, a dose map, and a film to determine position and dose accuracy using the red or green lasers. Coronal and sagittal slices may be analyzed.

\*Only available in the RIT Complete software package.

## Image Quality Tests

- Noise
- Contrast
- Resolution
- Uniformity
- Geometric Accuracy
- Geometric Distortion
- CT Number to Density
- Pin Prick, Erase, and ROI tool



## Built-In Features

-  RITtrend™ statistical database for reporting and trending measurements over time
-  PDF report exports for every analysis routine

**CLICK TO REQUEST A DEMO  
& UPGRADE YOUR TG-148  
QA CAPABILITIES TODAY**



**RADIMAGE.COM**

+1.719.590.1077, Opt. 4 // sales@radimage.com // Connect with us on social media @RIT4QA

©2021, Radiological Imaging Technology, Inc.

TomoTherapy® and Radixact® are registered trademarks of Accuray, Inc.

Article type : Research Article

## **Clinical Assessment of a Biophysical Model for Distinguishing Tumor Progression from Radiation Necrosis**

Ammoren E. Dohm<sup>1</sup>, Tanner M. Nickles<sup>2</sup>, Caroline E. Miller<sup>2</sup>, Haley J. Bowers<sup>2</sup>, Michael I. Miga<sup>3</sup>, Albert Attia<sup>4,5</sup>, Michael D. Chan<sup>1,6</sup>, Jared A. Weis<sup>2,6</sup>

<sup>1</sup>Department of Radiation Oncology, Wake Forest School of Medicine

<sup>2</sup>Department of Biomedical Engineering, Wake Forest School of Medicine

<sup>3</sup>Department of Biomedical Engineering, Vanderbilt University

<sup>4</sup>Department of Radiation Oncology, Vanderbilt University Medical Center

<sup>5</sup>Bon Secours Mercy Health St. Francis Cancer Center

<sup>6</sup>Comprehensive Cancer Center, Wake Forest Baptist Medical Center

### **Corresponding Author:**

Jared A. Weis, Ph.D.

575 N. Patterson Ave

Suite 530

Winston-Salem, NC 27101

Phone: (336) 716-0740

E-mail: [jweis@wakehealth.edu](mailto:jweis@wakehealth.edu)

### **Running Title:**

Tumor progression and radiation necrosis

### **Abstract**

This article has been accepted for publication and undergone full peer review but has not been through the copyediting, typesetting, pagination and proofreading process, which may lead to differences between this version and the [Version of Record](#). Please cite this article as [doi: 10.1002/MP.14999](https://doi.org/10.1002/MP.14999)

This article is protected by copyright. All rights reserved

**Purpose:** The efficacy of an imaging-driven mechanistic biophysical model of tumor growth for distinguishing radiation necrosis from tumor progression in patients with enhancing lesions following stereotactic radiosurgery (SRS) for brain metastasis is validated.

**Methods:** We retrospectively assessed the model using 73 patients with 78 lesions and histologically confirmed radiation necrosis or tumor progression. Post-contrast T1-weighted MRI images were used to extract parameters for a mechanistic reaction-diffusion logistic growth model mechanically coupled to the surrounding tissue. The resulting model was then used to estimate mechanical stress fields, which were then compared with edema visualized on FLAIR imaging using DICE similarity coefficients. DICE, model, and standard radiographic morphometric analysis parameters were evaluated using a receiver operating characteristic (ROC) curve for prediction of radiation necrosis or tumor progression. Multivariate logistic regression models were then constructed using mechanistic model parameters or advanced radiomic features. An independent validation was performed to evaluate predictive performance.

**Results:** Tumor cell proliferation rate resulted in ROC AUC = 0.86, 95% CI: 0.76 – 0.95,  $p < 0.0001$ , 74% sensitivity and 95% specificity) and DICE similarity coefficient associated with high stresses demonstrated an ROC AUC = 0.93, 95% CI: 0.86 – 0.99,  $p < 0.0001$ , 81% sensitivity and 95% specificity. In a multivariate logistic regression model using an independent validation dataset, mechanistic modeling parameters had an ROC AUC of 0.95, with 94% sensitivity and 96% specificity.

**Conclusions:** Imaging-driven biophysical modeling of tumor growth represents a novel method for accurately predicting clinically significant tumor behavior.

**Keywords:** brain metastasis, stereotactic radiosurgery, radiation necrosis, tumor progression, computational model

## Introduction

Brain metastases (BM) are a significant cause of morbidity and mortality in an estimated 10-30% of cancer patients with more patients being affected each year as many

primary cancer survival rates improve<sup>1,2</sup>. An increasing number of these brain metastasis are being treated with stereotactic radiosurgery (SRS)<sup>3</sup>. Despite treatment with SRS, patients can experience local failure rates as high as 27% to 33%<sup>4-6</sup> and an incidence of radiation necrosis of 7 to 24%<sup>7,8</sup>. Radiation necrosis is thought to result from an inflammatory cascade initiated by the action of reactive oxygen species, leading to small vessel injury, vasogenic edema, and coagulative necrosis, which can result in mass effect, the need for prolonged steroid use, and even surgical intervention.

Both tumor progression and radiation necrosis can occur anytime from 3 months following SRS to several years later. Accurate diagnosis of these lesions presents enormous clinical challenges as clinical symptoms and radiographic findings for radiation necrosis and tumor progression are often indistinguishable; see Figure 1. These sequelae are often monitored with serial magnetic resonance imaging (MRI) as radiation necrosis often spontaneously regresses with time, however, this monitoring can lead to delay in subsequent therapy<sup>9</sup>. Further, misdiagnosis can lead to disease progression, improper discontinuation of systemic therapy, steroid use, surgical intervention, or inaccurate prognosis. A biopsy is the gold standard for accurate diagnosis but introduces considerable risk and is often not possible due to the patient's condition or lesion location. Attempts have been made to utilize one or multiple non-invasive modalities, but achieving an accurate diagnosis utilizing existing non-invasive modalities remains difficult and unreliable<sup>10-12</sup>.

Thus, an unmet need exists for clear, non-invasive, diagnostic imaging modalities to accurately differentiate between radiation necrosis and tumor progression. In recent work, we introduced a biophysical tumor growth model coupled to longitudinal lesion changes observed from MRI data following SRS for brain metastasis that showed preliminary promise as such a method in a limited ten patient cohort proof-of-concept analysis<sup>13</sup>. As a follow-up to that preliminary study, in this work we seek to evaluate this mechanistic biophysical modeling method within a separate and larger scale cohort of patients with pathologically confirmed radiation necrosis or tumor progression. We additionally seek to compare the predicative accuracy of the mechanistic model-based method to a radiomics method for radiographic assessment of image morphometric and texture features.

## Methods

### *Patient imaging data*

A prospectively maintained database at our institution with 73 patients with 78 brain metastasis treated with SRS and histologically confirmed radiation necrosis or tumor progression were retrospectively assessed under a Wake Forest Institutional Review Board approved study. A previously developed mechanistic modeling approach was used to estimate biophysical properties of lesion expansion based on conventional MR imaging<sup>13</sup>. Patients treated with SRS were followed with serial imaging at the discretion of the care team, most often at 1-3 month intervals, to evaluate for enhancement and radiographic evidence of recurrence/progression or necrosis. All patients in this database exhibited lesion growth on follow-up imaging and were histologically confirmed for tissue diagnosis; see Table 1. Images were acquired during the course of routine clinical care and as such are not standardized between patients. We report the median value of imaging acquisition parameters with T1-weighted images acquired with 0.47mm x 0.47 mm x 2 mm voxel size, 3.4 ms TE, 8.7 ms TR, 450 ms TI, and 20° flip angle. FLAIR/T2 images were acquired with 512x512x44 acquisition matrix, 0.47mm x 0.47 mm x 3.5 mm voxel size, 136 ms TE, 8816 ms TR, 2750 ms TI, and 90° flip angle. Images were subsequently minimally post-processed with the two T1-weighted scans histogram normalized and lesion segmentations manually performed (ITK-Snap)<sup>14</sup>.

T1-weighted imaging data from two serial imaging examination time points immediately prior to pathological diagnosis and FLAIR MR imaging data from the imaging examination time point immediately prior to pathological diagnosis were used as input data. Prior to analysis, all MR images were longitudinally co-registered and central-slice images through the mid-point of the lesion were extracted for subsequent mechanistic modeling analysis. T1-weighted and FLAIR enhancement lesion regions-of-interest were manually segmented for each patient.

### *Mechanistic modeling analysis*

For mechanistic modeling analysis, a previously-developed reaction-diffusion logistic growth

model mechanically coupled to the surrounding tissue was used to extract biophysical model-based parameters of tumor cell proliferation rate and diffusion coefficient<sup>13,15,16</sup>; see Figure 2. While a brief description for the methodological implementation of this mechanistic modeling approach follows, a more complete description is provided as supplementary material and in our previous proof-of-concept work<sup>13</sup>. The coupled set of partial differential equations governing the model are shown in Equations [1] - [3] which describe tumor cell proliferation, mechano-inhibitory tumor cell diffusion, and deformation mass effect due to mechanical solid stress fields imparted by an expanding lesion. Equation [1] models the spatiotemporal rate of change of tumor cells ( $N$ ) as the summation of cell diffusion and logistic growth, governed by the tumor cell proliferation rate,  $k$ , and the maximal cellular carrying capacity,  $\theta$ . Equation [2] defines the apparent local cellular diffusion coefficient,  $D$ , in terms of the tumor cell diffusion coefficient in the absence of stress,  $D_0$ , tissue distortional energy,  $\sigma_{vm}$ , and coupling constant,  $\gamma$ . Eq. [3] describes linear elastic, isotropic mechanical equilibrium subject to an external expansive force given by changes in tumor cell number and coupling constant,  $\lambda$ . For a more complete discussion of the model and implementation, see the supplementary materials.

$$\frac{\partial N(x,t)}{\partial t} = \nabla \cdot (D \nabla N(x,t)) + kN(x,t) \left(1 - \frac{N(x,t)}{\theta}\right) \quad [1]$$

$$D = D_0 e^{-\gamma \sigma_{vm}(x,t)} \quad [2]$$

$$\nabla \cdot \sigma - \lambda \nabla N = 0 \quad [3]$$

The mechanistic model parameters of  $D_0$  and  $k$  were estimated for all patients by fitting the model to observed changes in estimated tumor cellularity based on segmented areas of post-contrast  $T1$ -weighted MR enhancement observed during both serial imaging time points. Following model-to-data parameter fitting with the  $T1$ -weighted MR images, the mechanical solid stress field imparted by the expanding lesion is estimated by the model. Based on our prior proof-of-concept study that showed a correlation between mechanical stress and the visualized edema front for tumor progression but not radiation necrosis<sup>13</sup>, the Dice similarity coefficient<sup>17</sup> was used to quantify similarity of the model-estimated stress field

at a range of stress isocontours with the edema front visualized and segmented from FLAIR imaging as a measure of mechanical stress-induced edema. Dice coefficient analysis is a measure of region overlap that varies between 0 and 1, with 0 being no overlap and 1 being 100% overlap. We quantify the degree of correlation between the model-estimated stress and the segmented FLAIR lesion with Dice coefficient. ROC analysis can then be used to define optimal cutoffs in the Dice coefficient that discriminate between tumor and necrosis. In summary, the mechanistic biophysical model fits proliferation rate ( $k$ ) and tumor cell diffusion coefficient ( $D_0$ ) from  $T1$ -weighted images, estimates a mechanical stress field due to tumor growth at the final time point, and Dice coefficient is used to evaluate the similarity overlap between the stress field and edema visualized from FLAIR imaging at the last time point.

#### *Univariate prediction analysis*

Each mechanistic model-based parameter (tumor cell proliferation rate, tumor cell diffusion coefficient, and stress isocontour Dice similarity coefficients) was evaluated using a receiver operating characteristic (ROC) curve for prediction of tumor progression versus radiation necrosis. The area under the curve (AUC), sensitivity, and specificity were used to evaluate univariate predictors. To determine sensitivity and specificity we defined cutoff values to specify the decision threshold between tumor progression and radiation necrosis using the Youden index<sup>18,19</sup>, defined as the vertical distance between the line of identity and the point on the ROC curve. Optimal cutoff value thresholds were selected by choosing the point on the ROC curve which maximizes the Youden index, maximizing the difference between the true positive rate (TPR) and the false positive rate (FPR). In addition, we evaluated standard radiographic morphometric analysis parameters previously used for prediction of tumor progression versus radiation necrosis, including the change in the longest dimension of the lesion from  $T1$ -weighted MR imaging time points and the FLAIR/ $T1$  lesion area quotient.

#### *Radiomics analysis*

An open-source software platform, Cancer Imaging Phenomics Toolkit (CaPTk)<sup>20</sup> was used to extract radiomics feature data for all imaging data for each patient (*T1*-weighted images at both time points and FLAIR images at the final time point). *T1*-weighted and FLAIR images for each patient were bias field corrected<sup>21</sup> and intensity normalized by histogram-matching<sup>22</sup> to a common corresponding modality patient image and regions-of-interest corresponding to the lesion were manually segmented in three dimensions for each image volume. Radiomics feature data corresponding to intensity histogram-based, volumetric, morphologic, and texture (GLCM – gray-level co-occurrence matrix, GLRM – gray level run length matrix, GLSZM – gray-level size zone matrix, NGTDM – neighborhood grey tone difference matrix, LBP – local binary patterns) features were extracted, with 360 features for each image (*T1*-weighted MR at both time points and FLAIR MR at the final time point) for a total of 1,080 radiomics features for each patient. A fixed bin count approach was used for radiomics histogram discretization with the default recommended parameters from CaPTK (10 bins).

#### *Multivariate prediction analysis*

To explore our mechanistic modeling approach to more traditional radiomics image analysis, we constructed multivariate logistic regression models to combine individual parameters to build signatures for predicting radiation necrosis or tumor progression. Two multivariate prediction models were built:  $m_{mechanistic}$  and  $m_{radiomics}$  which reflect separate multivariate logistic regression models that differ based on the source of independent variables. These models are built with input data from either mechanistic modeling parameters only or radiomics features only. Mechanistic modeling metrics include the model-estimated proliferation rate ( $k$ ), model-estimated tumor cell diffusion coefficient ( $D_0$ ), and Dice similarity coefficients across a range of five stress isocontours from low to high stress. Multivariate logistic regression models are used to assess relative model significance in predicting the probability of either tumor recurrence or radiation necrosis based on a linear weighted summation of independent variables and regression coefficients. As there was a significantly larger number of features extracted relative to the number of patients, we used the least absolute shrinkage and selection operator (LASSO)<sup>23</sup> regularized logistic

Accepted Article

regression model to identify significant features for prediction for the regression models. Without feature reduction, regression models have a significant risk of overfitting due to the significant degree of parameterization. To identify an optimal reduced feature set using LASSO, we follow the widely recommended practice of K-fold cross-validation to select an optimal LASSO regularization parameter, lambda, for feature selection that minimizes cross-validation error<sup>23-26</sup>. Using a 10-fold cross-validation design, we examine a range of lambda tuning parameters by training on the remainder of data and testing on the held-out data within each fold. A cross-validation error curve is then generated that reflects average prediction error at each lambda value. We then select the lambda value that minimizes average prediction error over the 10-fold cross-validation process and then re-run LASSO on the entire dataset using the selected optimal lambda value. Features with non-zero coefficients are then identified as the reduced feature set. The optimal number of features was automatically determined through the selection of the optimal LASSO regularization parameter, lambda, which was selected as the value which minimized the estimated expected deviance across folds in 10-fold cross-validation. The LASSO method was used to automatically determine the optimal features to minimize cross-validation error across folds rather than maximize performance within folds such that the optimal model reduces the chance of overfitting. To assess predictive performance, multivariate logistic regression models were then built without LASSO using the optimal reduced feature set and receiver operating characteristic (ROC) curves were generated with optimal cutoff thresholds specified by the Youden index. The area under the curve (AUC), sensitivity, and specificity were calculated to evaluate prediction performance. As overfitting the dataset is possible when using all available patient data, it is important to also test out-of-sample regression model performance. We performed an independent validation regression analysis whereby we partitioned our dataset into two fully independent groups to include a training dataset and a separate validation dataset. We used an 85%/15% random split to partition data into a training dataset and a validation dataset and built regression models ( $m_{mechanistic}$  and  $m_{radiomics}$ ) based only on the training dataset using the optimal reduced feature sets selected using LASSO with 10-fold cross-validation. Predictive performance of multivariate models

was then assessed using ROC curve analysis only on the validation dataset. To ensure robustness against random sampling bias, we repeated this process for 100 iterations using a repeated random subsampling validation design in which we record AUC, sensitivity, and specificity for each iteration of the 85%/15% random split and report mean and 95% confidence intervals.

## Results

A total of 73 patients with 78 lesions were identified who met our inclusion criteria. Patient and radiation treatment characteristics are summarized in Table 1. The most common primary histology was non-small cell lung cancer, followed closely by breast cancer. SRS for all patients was delivered using Gamma Knife for all patients with 95% being treated without prior irradiation and 88% being treated without prior WBRT. Median tumor volume was 2.72 cm<sup>3</sup> (0.021-16.99); small tumors were not excluded; see Table 1.

### *Univariate prediction analysis*

Standard radiographic morphometric analysis of the serial post-contrast *T1*-weighted enhanced and FLAIR images reflected fair ability to differentiate between tumor progression and radiation necrosis for the change in the longest dimension of the lesion (ROC AUC = 0.73, 95% CI: 0.61 – 0.85,  $p = 0.0009$ , 74% sensitivity and 63% specificity), change in lesion volume (ROC AUC 0.61, 95% CI: 0.47 – 0.75,  $p = 0.1262$ , 43% sensitivity and 64% specificity), and FLAIR/*T1* lesion quotient (ROC AUC = 0.55, 95% CI: 0.41 – 0.69,  $p = 0.4723$ , 77% sensitivity and 43% specificity). Conversely, parameters derived from the imaging-driven mechanistic model were able to differentiate lesion etiology with excellent accuracy for tumor cell proliferation rate (ROC AUC = 0.86, 95% CI: 0.76 – 0.95,  $p < 0.0001$ , 74% sensitivity and 95% specificity) and Dice similarity coefficient associated with high model-estimated mechanical stresses (ROC AUC = 0.93, 95% CI: 0.86 – 0.99,  $p < 0.0001$ , 81% sensitivity and 95% specificity); see Figure 3 and Table 2.

### *Multivariate prediction analysis*

Multivariate logistic regression analysis shows that multivariate predictive models have an improved ability to predict tumor progression and radiation necrosis over univariate parameters. In this work, two different statistical models were created that differ based on the source of independent variables,  $m_{mechanistic}$  and  $m_{radiomics}$ . The LASSO method was used to select an optimal reduced feature set to reduce the chance for overfitting. For  $m_{mechanistic}$ , the LASSO selected features were model-estimated tumor cell diffusion coefficient ( $D_0$ ) and Dice similarity coefficients of the highest three stress isocontours. For  $m_{radiomics}$ , the LASSO selected features were morphologic short axis ellipse diameter, morphologic equivalent spherical radius, GLSZM zone percentage, and NGTDM strength from the final  $T1$ -weighted image and 90 percentile intensity from the FLAIR image. When multivariate logistic regression models were fit to all of the available patient data, the mechanistic regression model,  $m_{mechanistic}$ , exhibited a ROC AUC of 0.97 (95% CI: 0.92 – 1.0), with sensitivity and specificity of 95% and 96%, respectively. The radiomics regression model,  $m_{radiomics}$ , had a ROC AUC of 0.82 (95% CI: 0.71 – 0.92), with sensitivity and specificity of 95% and 62%, respectively; see Figure 4 and Table 2.

As fitting logistic regression models to all available data can potentially lead to overfitting the data, which results in statistical models that perform poorly on novel out-of-training set data, we also assessed regression model performance by using an independent training/validation dataset analysis with repeated random subsampling validation. In this setting, the mechanistic model-based regression model,  $m_{mechanistic}$ , had a mean ROC AUC of 0.95 (CI: 0.94-0.97), with 94% (CI: 92-95) sensitivity and 96% (CI: 94-98) specificity. The radiomics regression model,  $m_{radiomics}$ , had a mean ROC AUC of 0.77 (CI: 0.75-0.80), with 86% (CI: 83-89) sensitivity and 73% (CI: 69-78) specificity; see Table 2.

## Discussion

Brain metastasis patients are not always candidates for surgical resection due to eloquent location of some metastases and limited life expectancy of some patients<sup>27</sup>. This clinical dilemma has led to several attempts to find successful non-invasive diagnostic techniques to distinguish radiation necrosis from tumor progression. Some populations have been shown to be at increased risk of radiation necrosis including patients with larger

lesions, those treated with concurrent immunotherapy, or those receiving a second treatment of SRS<sup>28-30</sup>. In these patients, imaging changes can often be treated expectantly as radiation necrosis until proven otherwise. In standard-risk patients, however, the limited efficacy of contrast-enhanced MRI follow-up imaging in patients with brain metastasis treated with SRS has led to the investigation of adjunctive methods including various positron emission tomography (PET) techniques, magnetic resonance spectroscopy, and perfusion-weighted MRI (PWI); however, these results have had limited success<sup>12,31,32</sup>.

The emerging field of radiomics and machine learning has shown recent promise for differentiating radiation necrosis from tumor progression<sup>33,34</sup>. One recent study by Peng et al found that 51 radiomic features extracted using an in-house software could be used in 66 patients with 77 confirmed lesions, to differentiate tumor progression from radiation necrosis with a sensitivity and specificity of 65.38% and 86.67%, respectively, with an area under the curve of 0.81<sup>34</sup>. Interestingly, our radiomics regression model showed comparable predictive performance. In our study, LASSO identified important features describing the size/shape of the lesion (short axis ellipse diameter, equivalent spherical radius), texture coarseness (GLSZM zone percentage), and image primitives (NGTDM strength) from the final *T1*-weighted image and intensity (90 percentile) from the FLAIR image and achieved ROC AUC of 0.77 in an independent validation setting.

One limitation of radiomics is the difficulty of associating biologic mechanisms with radiomic features, making widespread use and consistent results among independent datasets challenging. The biophysical mechanism-based model helps to overcome this weakness by parameterizing the biophysics of lesion growth and thus marries underlying mechanism to morphologic imaging features. Specifically, we utilize a reaction-diffusion model of tumor growth that includes mechanical coupling to the surrounding tissue stiffness, creating a mechanically-restricted cell diffusion growth model as described in previous work<sup>13</sup>. We relied on the assumption that the parameters of  $D_0$  (cellular diffusion coefficient) and  $k$  (cell proliferation rate) are significantly different in tumor growth versus radiation necrosis. We fit these parameters to “observed tumor cellularity” and use them to calculate a mechanical solid stress distribution, which is compared the observed edema using a Dice

similarity coefficient. Both cell proliferation rate and Dice similarity coefficient at high model-estimated mechanical stresses were accurately able to differentiate lesion etiology in the univariate predictive setting. Combining model parameters in a multivariate fashion further increased predictive ability. These findings confirm our underlying mechanistic assumptions that tumor progression will exhibit more cell proliferation and that the loading conditions of tumor growth have higher local distortional strain energy that results in edema. When a multivariate statistical model was created to explore the combination of biophysical parameters, it showed excellent predictive abilities.

While our biophysical modeling approach shows great promise for the ability to accurately model tumor growth within the mechanically restricted environment of brain parenchyma, this study has several important limitations. These are summarized below with a more complete discussion of technical limitations in a prior proof-of-concept study<sup>13</sup>. Lesion segmentation was manual and thus potentially introduces observer error and/or bias. The model also treats brain matter as a homogeneous isotropic elastic tissue despite the brain's mechanical heterogeneity. Future studies refining the model could incorporate such heterogeneity for potentially increased accuracy. In our study, mixed pathology was assumed as true progression; although this mirrors clinical treatment paradigms, an ideal model would account for and identify this heterogeneity. Additionally, there is potential for overestimation of the impact of individual LASSO selected features in this study. LASSO, and more generally all sparsity-inducing feature reduction algorithms, are not uniformly algorithmically stable<sup>35,36</sup>. Future studies are needed to validate the impact and predictive accuracy of the selected features. Finally, the sample size of 73 patients at a single site is a limitation in this study. It will be important in future studies to examine training the multivariate regression models with a significantly larger amount of data from additional centers and MRI scanners to robustly evaluate reproducibility and clinical efficacy.

We demonstrate that an imaging-driven biophysical model is able to accurately differentiate radiation necrosis from tumor progression, prior to pathological diagnosis. These results suggest that a mechanism-based modeling method has the potential to be a powerful tool for interpreting follow-up imaging in a significant patient population and

outperformed standard radiographic analysis in our dataset. The methods presented in this study could vastly increase the accuracy and timeliness of diagnosis and pave the way for advancements in brain metastasis treatment allowing for improved tumor control and survival. Further, our work supports the emerging concept that biophysical modeling can provide a valuable physics-based mechanistic signature using computational reactive-diffusive tumor growth biophysics as a mechanistic filter to evaluate imaging data. This is in contrast to functional molecular or imaging-physics contrast signatures as evaluated by radiomic evaluation methods, which have been shown to be incomplete for differentiating radiation necrosis from tumor progression.

### **Conflicts of Interest**

The authors have no relevant conflicts of interest to disclose.

### **Acknowledgements**

This work is supported by the National Institutes of Health-National Cancer Institute: K25CA204599, P30CA012197; RSNA Medical Student Research Grant; National Science Foundation Research Experiences for Undergraduates 1559700; and the VISE Seed Grant Program.

### **Data Availability Statement**

The data that support the findings of this study are available from the corresponding author upon reasonable request.

### **References**

1. Smith DR, Bian Y, Wu CC, et al. Natural history, clinical course and predictors of interval time from initial diagnosis to development of subsequent NSCLC brain metastases. *J Neurooncol.* 2019;143(1):145-155.
2. Smedby KE, Brandt L, Backlund ML, Blomqvist P. Brain metastases admissions in Sweden between 1987 and 2006. *Br J Cancer.* 2009;101(11):1919-1924.

- Accepted Article
3. Halasz LM, Weeks JC, Neville BA, Taback N, Punglia RS. Use of stereotactic radiosurgery for brain metastases from non-small cell lung cancer in the United States. *Int J Radiat Oncol Biol Phys.* 2013;85(2):e109-116.
  4. Sahgal A, Aoyama H, Kocher M, et al. Phase 3 trials of stereotactic radiosurgery with or without whole-brain radiation therapy for 1 to 4 brain metastases: individual patient data meta-analysis. *Int J Radiat Oncol Biol Phys.* 2015;91(4):710-717.
  5. Soliman H, Das S, Larson DA, Sahgal A. Stereotactic radiosurgery (SRS) in the modern management of patients with brain metastases. *Oncotarget.* 2016;7(11):12318-12330.
  6. Tsao M, Xu W, Sahgal A. A meta-analysis evaluating stereotactic radiosurgery, whole-brain radiotherapy, or both for patients presenting with a limited number of brain metastases. *Cancer.* 2012;118(9):2486-2493.
  7. Chin LS, Ma L, DiBiase S. Radiation necrosis following gamma knife surgery: a case-controlled comparison of treatment parameters and long-term clinical follow up. *J Neurosurg.* 2001;94(6):899-904.
  8. Minniti G, Clarke E, Lanzetta G, et al. Stereotactic radiosurgery for brain metastases: analysis of outcome and risk of brain radionecrosis. *Radiat Oncol.* 2011;6:48.
  9. Verma N, Cowperthwaite MC, Burnett MG, Markey MK. Differentiating tumor recurrence from treatment necrosis: a review of neuro-oncologic imaging strategies. *Neuro Oncol.* 2013;15(5):515-534.
  10. Chao ST, Ahluwalia MS, Barnett GH, et al. Challenges with the diagnosis and treatment of cerebral radiation necrosis. *Int J Radiat Oncol Biol Phys.* 2013;87(3):449-457.
  11. Chuang MT, Liu YS, Tsai YS, Chen YC, Wang CK. Differentiating Radiation-Induced Necrosis from Recurrent Brain Tumor Using MR Perfusion and Spectroscopy: A Meta-Analysis. *PLoS One.* 2016;11(1):e0141438.
  12. Detsky JS, Keith J, Conklin J, et al. Differentiating radiation necrosis from tumor progression in brain metastases treated with stereotactic radiotherapy: utility of intravoxel incoherent motion perfusion MRI and correlation with histopathology. *J Neurooncol.* 2017;134(2):433-441.
  13. Narasimhan S, Johnson HB, Nickles TM, et al. Biophysical model-based parameters to classify tumor recurrence from radiation-induced necrosis for brain metastases. *Med Phys.* 2019;46(5):2487-2496.

- Accepted Article
14. Yushkevich PA, Piven J, Hazlett HC, et al. User-guided 3D active contour segmentation of anatomical structures: significantly improved efficiency and reliability. *Neuroimage*. 2006;31(3):1116-1128.
  15. Weis JA, Miga MI, Arlinghaus LR, et al. Predicting the Response of Breast Cancer to Neoadjuvant Therapy Using a Mechanically Coupled Reaction-Diffusion Model. *Cancer Res*. 2015;75(22):4697-4707.
  16. Weis JA, Miga MI, Arlinghaus LR, et al. A mechanically coupled reaction-diffusion model for predicting the response of breast tumors to neoadjuvant chemotherapy. *Phys Med Biol*. 2013;58(17):5851-5866.
  17. Dice LR. Measures of the amount of ecologic association between species. *Ecology*. 1945;26(3):297-302.
  18. Perkins NJ, Schisterman EF. The inconsistency of "optimal" cutpoints obtained using two criteria based on the receiver operating characteristic curve. *Am J Epidemiol*. 2006;163(7):670-675.
  19. Youden WJ. Index for rating diagnostic tests. *Cancer*. 1950;3(1):32-35.
  20. Davatzikos C, Rathore S, Bakas S, et al. Cancer imaging phenomics toolkit: quantitative imaging analytics for precision diagnostics and predictive modeling of clinical outcome. *J Med Imaging (Bellingham)*. 2018;5(1):011018.
  21. Tustison NJ, Avants BB, Cook PA, et al. N4ITK: improved N3 bias correction. *IEEE Trans Med Imaging*. 2010;29(6):1310-1320.
  22. Nyul LG, Udupa JK, Zhang X. New variants of a method of MRI scale standardization. *IEEE Trans Med Imaging*. 2000;19(2):143-150.
  23. Tibshirani R. Regression shrinkage and selection via the lasso: a retrospective. *Journal of the Royal Statistical Society: Series B (Statistical Methodology)*. 2011;73(3):273-282.
  24. Zou H, Hastie T, Tibshirani R. On the "degrees of freedom" of the lasso. *The Annals of Statistics*. 2007;35(5):2173-2192.
  25. Tibshirani R. Regression shrinkage and selection via the lasso. *Journal of the Royal Statistical Society: Series B (Methodological)*. 1996;58(1):267-288.
  26. Greenshtein E, Ritov YA. Persistence in high-dimensional linear predictor selection and the virtue of overparametrization. *Bernoulli*. 2004;10(6):971-988.

27. Ellis TL, Neal MT, Chan MD. The role of surgery, radiosurgery and whole brain radiation therapy in the management of patients with metastatic brain tumors. *Int J Surg Oncol*. 2012;2012:952345.
28. Dohm A, McTyre ER, Okoukoni C, et al. Staged Stereotactic Radiosurgery for Large Brain Metastases: Local Control and Clinical Outcomes of a One-Two Punch Technique. *Neurosurgery*. 2018;83(1):114-121.
29. Lanier CM, Hughes R, Ahmed T, et al. Immunotherapy is associated with improved survival and decreased neurologic death after SRS for brain metastases from lung and melanoma primaries. *Neurooncol Pract*. 2019;6(5):402-409.
30. Shaw E, Scott C, Souhami L, et al. Single dose radiosurgical treatment of recurrent previously irradiated primary brain tumors and brain metastases: final report of RTOG protocol 90-05. *Int J Radiat Oncol Biol Phys*. 2000;47(2):291-298.
31. Kickingreder P, Dorn F, Blau T, et al. Differentiation of local tumor recurrence from radiation-induced changes after stereotactic radiosurgery for treatment of brain metastasis: case report and review of the literature. *Radiat Oncol*. 2013;8:52.
32. Tomura N, Kokubun M, Saginoya T, Mizuno Y, Kikuchi Y. Differentiation between Treatment-Induced Necrosis and Recurrent Tumors in Patients with Metastatic Brain Tumors: Comparison among (11)C-Methionine-PET, FDG-PET, MR Permeability Imaging, and MRI-ADC-Preliminary Results. *AJNR Am J Neuroradiol*. 2017;38(8):1520-1527.
33. Lohmann P, Kocher M, Ceccon G, et al. Combined FET PET/MRI radiomics differentiates radiation injury from recurrent brain metastasis. *Neuroimage Clin*. 2018;20:537-542.
34. Peng L, Parekh V, Huang P, et al. Distinguishing True Progression From Radionecrosis After Stereotactic Radiation Therapy for Brain Metastases With Machine Learning and Radiomics. *Int J Radiat Oncol Biol Phys*. 2018;102(4):1236-1243.
35. Xu H, Caramanis C, Mannor S. Sparse algorithms are not stable: A no-free-lunch theorem. *IEEE transactions on pattern analysis and machine intelligence*. 2011;34(1):187-193.
36. Bousquet O, Elisseeff A. Stability and generalization. *The Journal of Machine Learning Research*. 2002;2:499-526.

## Figure Legends

**Figure 1.** Serial imaging of lesions identified on follow-up after treatment of BM with SRS.

**Figure 2.** Schematic of mechanistic modeling framework for biophysical parameter estimation based on standard-of-care MR images for prediction of radiation necrosis and tumor progression.

**Figure 3.** ROC curves for univariate parameters from the biophysical model and standard radiographic morphometric analysis. The dotted line represents the line of identity.

**Figure 4.** ROC curves for multivariate logistic regression models combining individual parameters from with input data from radiomics features and mechanistic biophysical modeling parameters. LASSO regularized logistic regression was used to identify significant features for prediction. The dotted line represents the line of identity.

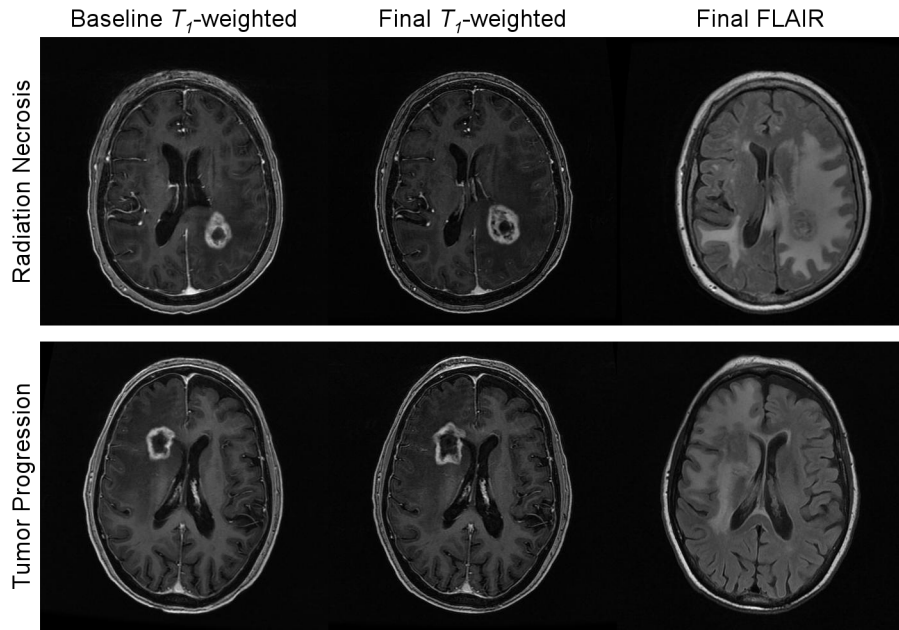
**Table 1.** Tumor and Treatment Characteristics

| <b>Characteristics</b>   | <b>Data</b>          |
|--|----------------------|
| No. Patients   | 73                   |
| No. Lesions  | 78                   |
| Lesion status (radiation necrosis/tumor recurrence)                | 31/47                |
| Median patient age at SRS (range)                                  | 54 (16-88)           |
| Male/Female  | 27/46                |
| No. of lesions treated (range)                                     | 1 (1-3)              |
| Median tumor volume (range)  | 2.72cc (0.021-16.99) |
| Median time between MRI scans                                      | 108 days             |
| Median time from SRS to 2nd imaging time point                     | 310 days             |
| <b>Primary Histology<br/>(radiation necrosis/tumor recurrence)</b> |                      |
| Lung Non-small Cell  | 29 (16/13)           |
| Breast   | 24 (7/17)            |
| Lung Small Cell  | 7 (3/4)              |
| Melanoma   | 6 (0/6)              |
| Colon Adenocarcinoma   | 5 (0/5)              |
| Thyroid  | 2 (2/0)              |
| Renal Cell Carcinoma   | 2 (2/0)              |
| Neuroendocrine   | 1 (1/0)              |
| Esophageal Adenocarcinoma  | 1 (0/1)              |
| Ovarian  | 1 (1/0)              |
| <b>Treatment Characteristics</b>                                   |                      |

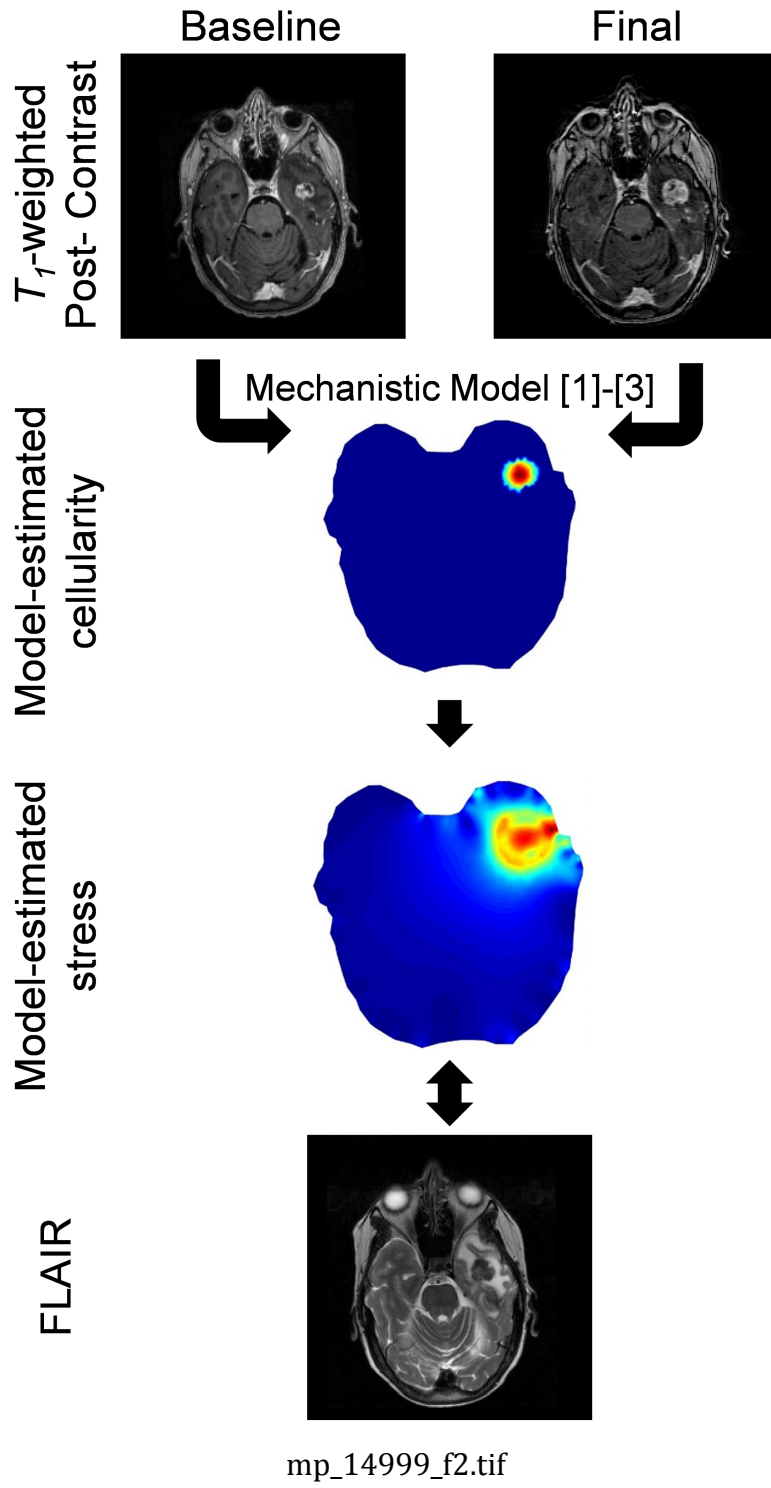
|  |               |
|--|---------------|
| Median total dose (range), Gy  | 18 (10-22)    |
| Median fractions (range)   | 1 (1-1)       |
| No. Treated with WBRT (%)  | 9 (12)        |
| No. with prior same-site SRS (%)   | 4(5)          |
| Median time from SRS to resection (range), d*  | 312 (45-1226) |
| <i>Abbreviations:</i> SRS = Stereotactic radiosurgery; WBRT = whole brain radiation therapy                    |               |
| *For lesions determined without pathology, time interval taken from SRS until date of maximum lesion diameter. |               |

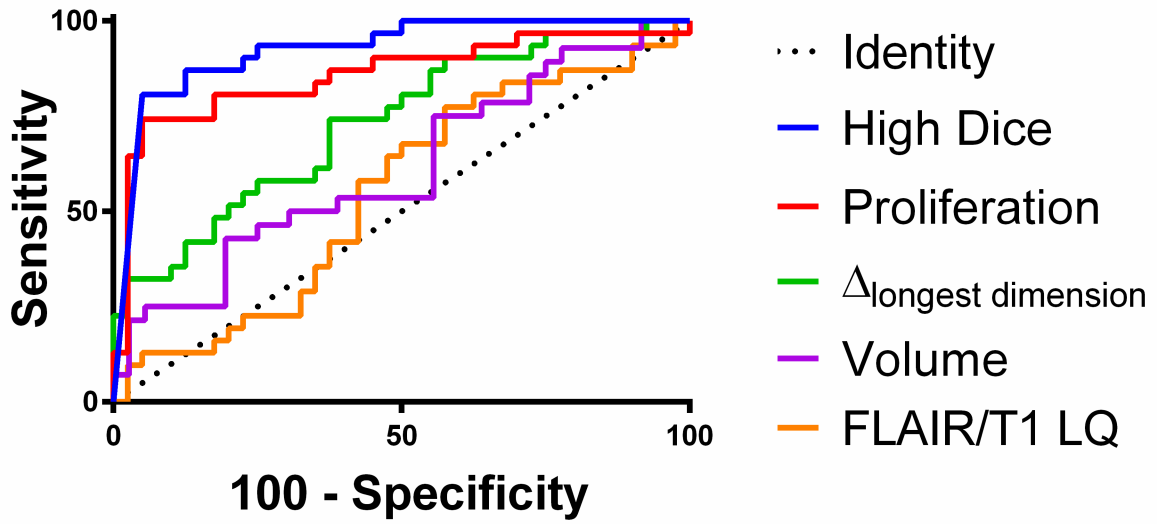
**Table 2.** Summary of ROC analyses

|  | <b>ROC AUC</b>     | <b>Sensitivity</b> | <b>Specificity</b> |
|--|--------------------|--------------------|--------------------|
| <b>Univariate</b>                            |                    |                    |                    |
| Lesion longest dimension                     | 0.73 (0.61 – 0.85) | 74%                | 63%                |
| Lesion change in volume                      | 0.61 (0.47 – 0.75) | 43%                | 64%                |
| FLAIR/ <i>T1</i> lesion quotient             | 0.55 (0.41 – 0.69) | 77%                | 43%                |
| proliferation rate                           | 0.86 (0.76 – 0.95) | 74%                | 95%                |
| High stress Dice similarity coefficient      | 0.93 (0.86 – 0.99) | 81%                | 95%                |
| <b>Multivariate</b>                          |                    |                    |                    |
| Radiomics features                           | 0.82 (0.71 – 0.92) | 95%                | 62%                |
| Mechanistic model features                   | 0.97 (0.92 – 1.0)  | 95%                | 96%                |
| <b>Multivariate – Independent validation</b> |                    |                    |                    |
| Radiomics features                           | 0.77 (0.75-0.80)   | 86% (83-89)        | 73% (69-78)        |
| Mechanistic model features                   | 0.95 (0.94-0.97)   | 94% (92-95)        | 96% (94-98)        |

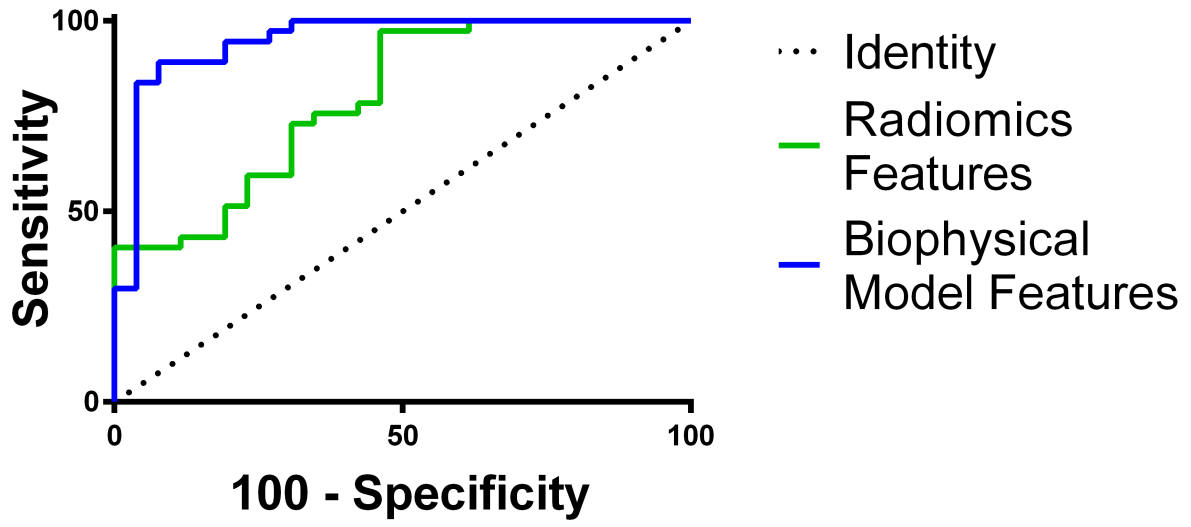


mp\_14999\_f1.tif





mp\_14999\_f3.tif



mp\_14999\_f4.tif